



# Optimum arrangement of PMs in surface-mounted PM machines: cogging torque and flux density harmonics

Vahid Zamani Faradonbeh<sup>1</sup> · Samad Taghipour Boroujeni<sup>1</sup> · Nouredine Takorabet<sup>2</sup>

Received: 5 November 2018 / Accepted: 10 January 2020  
© Springer-Verlag GmbH Germany, part of Springer Nature 2020

## Abstract

In surface-mounted PM machines, the cogging torque and the low-order harmonics of the air gap magnetic flux density are the main sources of the torque pulsation. These variables are strongly influenced by the distribution of the PMs on the surface of the rotor as well as the PMs' magnetization. In the presented work, the impact of the arrangement of the PMs and the PMs' magnetization pattern is studied. The PMs are arranged by some techniques such as PM arc optimization, PM shifting, PM segmentation and applying mixed material PMs. In addition, the parallel and radial magnetizations are investigated. For this purpose, the air gap flux density and cogging torque in the slotted SPM machines are predicted analytically. Using the analytical model and applying a direct search algorithm, the optimum arrangement for each technique is found. Moreover, to perform a multi-objective optimization, a weighted normalization method is applied. Finally, the proposed model and the obtained results are validated by finite element analysis.

**Keywords** Analytical modeling · Multi-objective optimization · PM segmentation · PM shifting · Surface-mounted PM motors · Parallel and radial magnetization

## List of symbols

$R_r$	Rotor radius (m)
$R_o$	Stator external radius (m)
$R_{PM}$	Permanent magnet region radius (m)
$R_s$	Stator bore radius (m)
$h_{PM}$	Height of permanent magnet (m)
$h_{slot}$	Height of stator slot (m)
$b_o$	Slot opening distance (m)
$\gamma_s$	Slot pitch angle
$\gamma_{so}$	Slot opening angle (rad)
$g$	Air gap length
$v_{i+}/v_{i-}$	Angle of right/left side of the $i$ th slot opening (rad)
$\tau_p$	Pole pitch angle (rad)
$\alpha$	The ratio of the PM arc to the pole pitch
$p$	Machine pole pairs
$T_{cog}$	Cogging torque (N m)
$\mu_0$	Free space permeability
$\theta_r$	Rotor angular position (rad)

$l_{stk}$	Machine stack length (m)
$B_{rem}$	Permanent magnet remnant flux density (T)
$r/\varphi$	Radial/angular values in the cylindrical coordinate

## Vectors

$\mathbf{a}_r/\mathbf{a}_\varphi$	The unitary, normal vectors in the radial/circumferential direction
$\mathbf{B}$	Magnetic flux density (Wb/m <sup>2</sup> )
$\mathbf{J}$	Real current density (A/m <sup>2</sup> )
$\mathbf{H}$	Magnetic field intensity (A/m)
$\mathbf{J}_m$	Volume EMC density (A/m <sup>2</sup> )
$\mathbf{J}_{ms}$	Surface EMC density (A/m)
$\mathbf{M}$	Magnetization vector (A/m)

## 1 Introduction

Surface-mounted PM (SPM) motors are attractive actuators because of their merits such as high power density, high efficiency and having a brushless structure. However, the torque pulsation is an important disadvantage of the SPM machine. The main problem of the pulsating torque is the vibration and acoustic noise [1]. The main source of the torque pulsation is the machine cogging torque and the harmonic contents of the air gap flux density. In particular,

✉ Samad Taghipour Boroujeni  
s.taghipour@sku.ac.ir

<sup>1</sup> Engineering Department, Shahrekord University, Shahrekord, Iran

<sup>2</sup> Université de Lorraine – GREEN, Nancy, France

the low-frequency harmonics of the air gap flux density have more influence on the torque pulsation. In the SPM machines, the cogging torque and the low-order harmonics of the air gap magnetic flux density are strongly influenced by the distribution of the PMs on the rotor surface [2]. For this purpose, different techniques such as PM shaping [3–7], pole arc optimization [8–12], PM shifting [9, 10] and PM segmentation [11, 12] methods are applied.

Although PM shifting method mitigates cogging torque, it destroys the half-odd symmetry in the PM magnetization. Consequently, undesired even-order harmonics of the air gap magnetic flux density are produced. This feature of the PM shifting method is disregarded in [9, 10].

In [13], PMs with different materials are integrated to achieve a desired air gap flux density distribution. This technique is termed as the mixed material PMs. The mixed magnet material method is employed to reduce the total harmonic distortion (THD) of the air gap flux density [13]. In addition, this technique is an effective method for reducing the machine torque ripple.

The PM segmentation is the other well-known method to reduce the cogging torque [11, 12]. However, it deteriorates the spectrum of the air gap flux density. This aspect of the PM segmentation method is not considered in [11]. In [12], finite element analysis (FEA) is used as the computational tool in the multi-objective optimization of the air gap magnetic flux density THD and the cogging torque, by means of the PM segmentation method. In [14], PWM arrangement of the PMs is applied to minimize the harmonics of the air gap flux density by using FEA and MATLAB optimization toolbox. However, the machine cogging torque is not considered in [14].

To study the effectiveness of the aforementioned techniques, analytical or FEA methods could be applied. Although the FEA is an accurate method, it needs heavy and time-consuming computations. This issue is not appropriate for the first design optimizations.

In the presented work, the analytical model for the slotted SPM machines with radial magnetization pattern proposed in [15] is extended to study the machines with more diversity in the magnetization. For this purpose, the mentioned PM arrangements are geometrically formulated. The adopted PM arrangements are PM shifting, mixed material PMs and PM segmentation. The developed model is used as the computational tool to optimize the arrangement of the radially or parallel-magnetized PMs. Since both cogging torque and THD of the air gap flux density are needed to be considered in the optimization process, a multi-objective optimization is implemented. In the optimization process, a direct search method is applied to find the optimum arrangement of PMs. Since the objective functions in the multi-objective optimization are not in the same unit, a weighted normalization technique is applied. It is shown that the PM shifting and the

mixed material PM result to the lowest cogging torque and the air gap flux density THD, respectively. Considering both flux density THD and machine cogging torque as the objective function the mixed material PM is found to be the best solution. Finally, the obtained results are validated by FEA.

## 2 Modeling of the PM arrangements

The PM magnetization is considered in the vector form as (1).

$$\mathbf{M}(r, \phi, \theta_r) = M_r(r, \phi, \theta_r)\mathbf{a}_r + M_\phi(r, \phi, \theta_r)\mathbf{a}_\phi \quad (1)$$

In all considered PM arrangements, the Fourier series of the radial and circumferential components of the PM magnetization are expressed as (2) and (3), respectively.

$$M_r(r, \phi, \theta_r) = \sum_{n=1,2,\dots}^{\infty} [M_{rcn} \cos(np(\phi - \theta_r)) + M_{rsn} \sin(np(\phi - \theta_r))] \quad (2)$$

$$M_\phi(r, \phi, \theta_r) = \sum_{n=1,2,\dots}^{\infty} [M_{\phi cn} \cos(np(\phi - \theta_r)) + M_{\phi sn} \sin(np(\phi - \theta_r))] \quad (3)$$

where the subscripts r,  $\phi$ , s, c and n denote the radial component, the circumferential component, the sine and cosine terms and the harmonics order, respectively. The base arrangement of PMs in the SPM machine is shown in Fig. 1a. The radial and parallel magnetization pattern of PM is shown in Fig. 1b. In the base arrangement, the arc angle of the PM is chosen as the optimization variable. The Fourier coefficients of the PMs magnetization in this arrangement is as (4) and (5) for the radial and parallel magnetization patterns, respectively, where X and Y are defined in (6).

$$(M_{rcn}, M_{rsn}) = \left( \frac{2B_{rem}}{\mu_0 n \pi} \sin\left(\frac{n\pi\alpha}{2}\right) (1 - \cos(n\pi)), 0 \right) \quad (4)$$

$$M_\phi(r, \phi, \theta_r) = 0$$

$$\begin{aligned} [M_{rcn}, M_{srn}] &= [(1 - \cos(n\pi))pB_{rem}(X + Y), 0] \\ [M_{\phi cn}, M_{\phi sn}] &= [0, (1 - \cos(n\pi))pB_{rem}(X - Y)] \end{aligned} \quad (5)$$

$$(X, Y) = \frac{1}{\mu_0 \pi} \left( \frac{\sin\left(\frac{(np+1)\alpha\pi}{2p}\right)}{np+1}, \frac{\sin\left(\frac{(np-1)\alpha\pi}{2p}\right)}{np-1} \right) \quad (6)$$

The PM radial and circumferential components of the magnetization function of the radial and parallel magnetization patterns are shown in Fig. 1c and d, respectively.

As well as the base arrangement of PMs (Fig. 1a), three other of the PM arrangements are considered in this study.

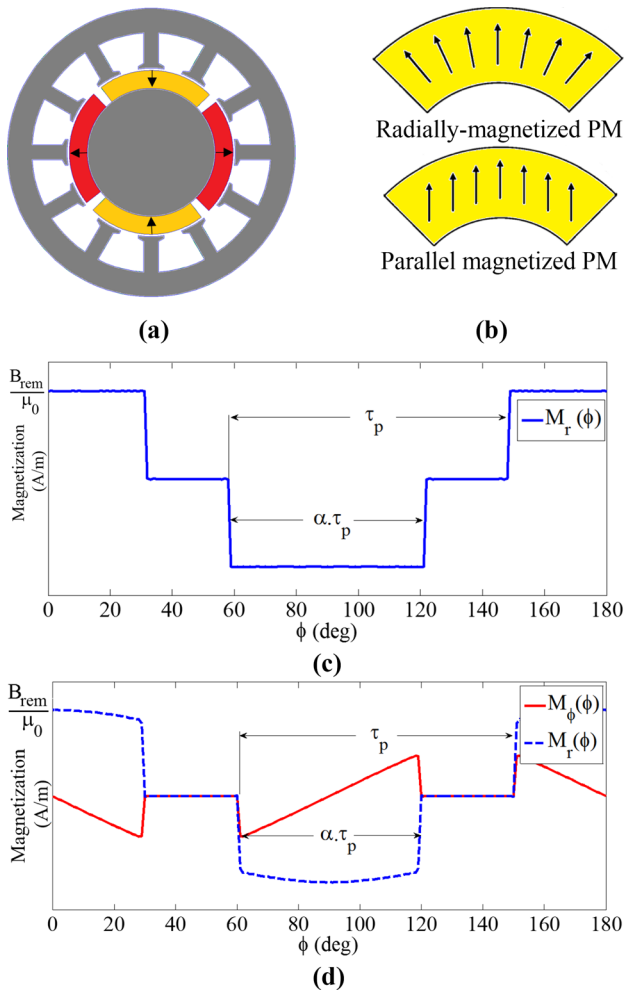


**Fig. 1** Base arrangement of PMs (a), radially and parallel-magnetized PMs (b), and magnetization functions in radial (c) and parallel (d) directions

In the first arrangement, as shown in Fig. 2a, the PMs are shifted with angle  $\alpha_0$ . The Fourier coefficients of the PM magnetization functions for the radially and parallel-magnetized PMs are obtained as (7) and (8), respectively.

$$\begin{aligned}
 [M_{rcn}, M_{rsn}] &= \frac{2B_{rem}}{\mu_0 n \pi} \sin\left(\frac{n\pi\alpha}{2}\right) (-1)^n [1 - \cos(n\pi\alpha_0), -\sin(n\pi\alpha_0)] \\
 [M_{\varphi cn}, M_{\varphi sn}] &= [0, 0]
 \end{aligned}
 \tag{7}$$

$$\begin{aligned}
 [M_{rcn}, M_{rsn}] &= (-1)^n \frac{2pB_{rem}}{\mu_0 \pi} (X + Y) [1 - \cos(n\pi\alpha_0), -\sin(n\pi\alpha_0)] \\
 [M_{\varphi cn}, M_{\varphi sn}] &= (-1)^n \frac{2pB_{rem}}{\mu_0 \pi} (X - Y) [-\sin(n\pi\alpha_0), 1 - \cos(n\pi\alpha_0)]
 \end{aligned}
 \tag{8}$$

The radial and circumferential components of the magnetization function of the radial and parallel magnetization patterns of the shifted PMs are illustrated in Fig. 2b and c, respectively.

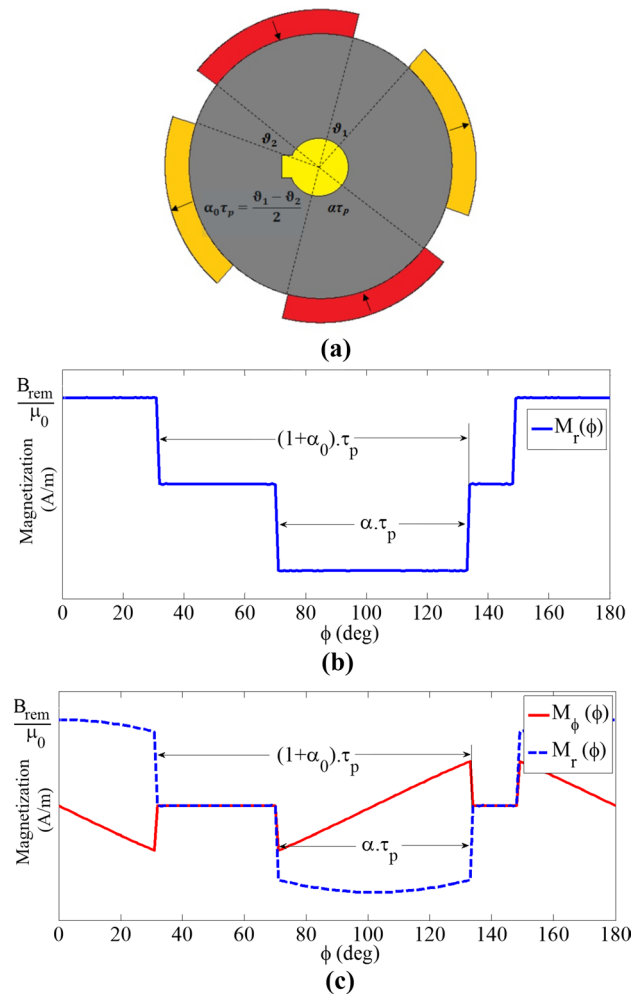


**Fig. 2** PM-shifted structure. Geometrical structure (a), the radial (b), and parallel (c) magnetization

In Fig. 3a, the rotor with the mixed material PMs is shown. In this arrangement, a strong PM with the remanence of  $B_{rem2}$  (NdFeB with high remnant flux density 1.2 T) is sandwiched between two weak PMs with the remanence of  $B_{rem1}$  (Ferrite with high remnant flux density 0.3 T). The aim of using mixed PM materials is decreasing the harmonic components of the PM magnetization to reach lower cogging torque and to obtain more sinusoidal back-EMF. The arc angles of the strong and weak PMs are as  $\alpha_1\tau_p$  and  $\alpha_2\tau_p$ , respectively, where  $\tau_p$  is the machine pole arc. The Fourier coefficients of the magnetization function of the mixed material magnetization function are reported in (9) and (10) for the radially and parallel-magnetized PMs, respectively.

$$\begin{aligned}
 M_{rcn} &= \frac{2(1 - \cos(n\pi))}{\mu_0 n \pi} \left( B_{rem1} \sin\left(\frac{n\pi(2\alpha_1 + \alpha_2)}{2}\right) \right. \\
 &\quad \left. + [B_{rem2} - B_{rem1}] \sin\left(\frac{n\pi\alpha_2}{2}\right) \right) \\
 M_{rsn} &= 0, \quad M_\varphi(r, \phi, \theta_r) = 0
 \end{aligned}
 \tag{9}$$

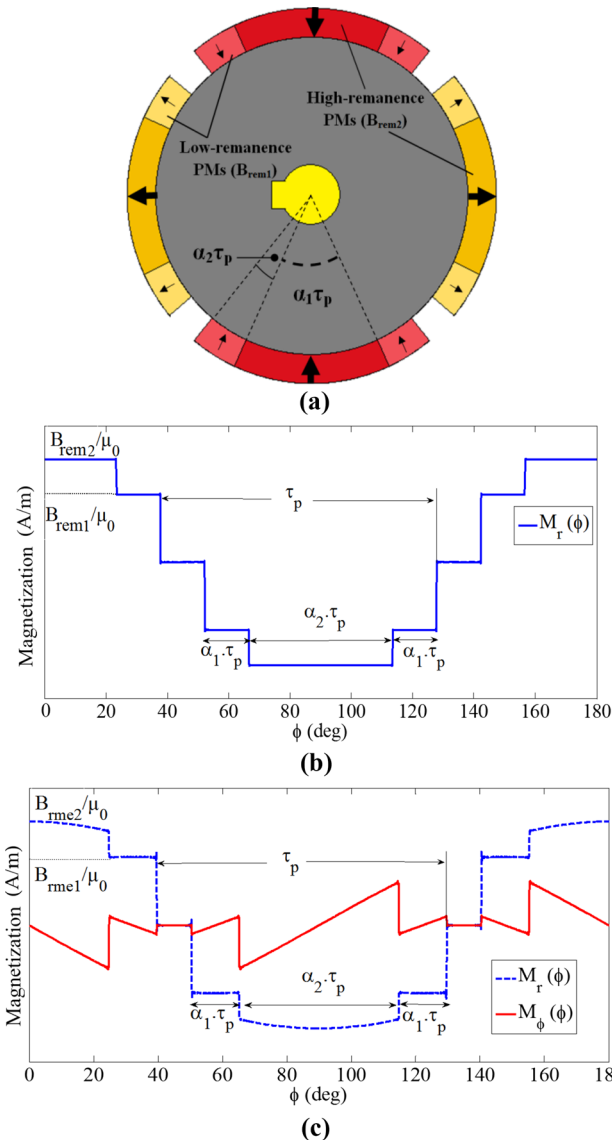


**Fig. 3** Rotor with the mixed material PMs. Geometrical structure (a), the radial (b) and parallel magnetization (c)

$$\begin{aligned}
 [M_{rn}, M_{rsn}] &= p(X + Y)(1 - \cos(n\pi)) \\
 &\quad \times \left[ B_{rem2} + 2B_{rem1} \cos\left(\frac{n\pi(\alpha_1 + \alpha_2)}{2}\right), 0 \right] \\
 [M_{\phi cn}, M_{\phi sn}] &= p(X - Y)(1 - \cos(n\pi)) \\
 &\quad \times \left[ 0, B_{rem2} + 2B_{rem1} \cos\left(\frac{n\pi(\alpha_1 + \alpha_2)}{2}\right) \right]
 \end{aligned} \tag{10}$$

The PM magnetization components of the radially and parallel-magnetized mixed material PMs are shown in Fig. 3b and c, respectively.

The structure of the PM-segmented rotor for two, three and four PM segments is shown in Fig. 4a–c, respectively. The PM magnetization components for the two-, three- and

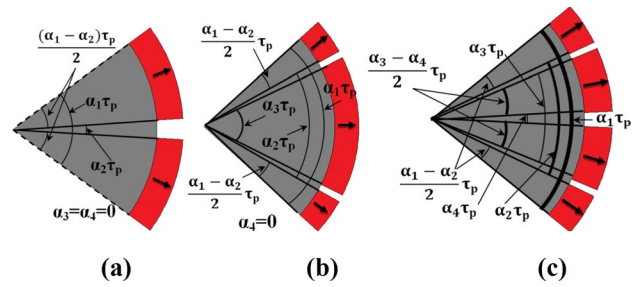


**Fig. 4** PM segmentation method for a two-, b three-, c four-segment structures

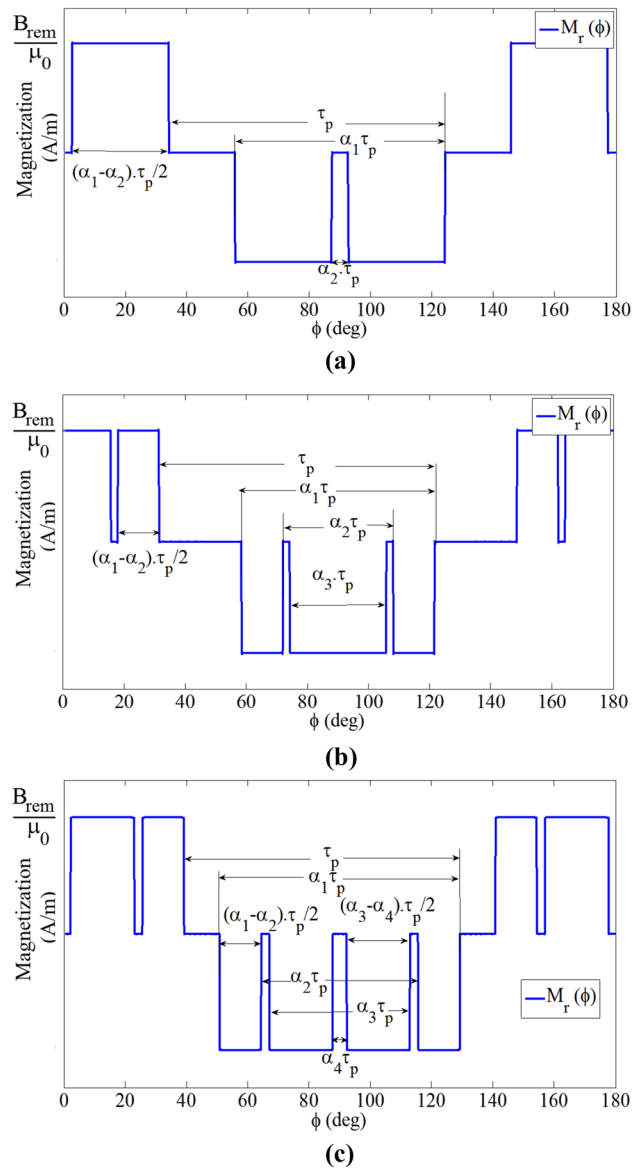


**Fig. 5** Magnetization of the structures with a two-, b three- and c four-segment radially magnetized PMs

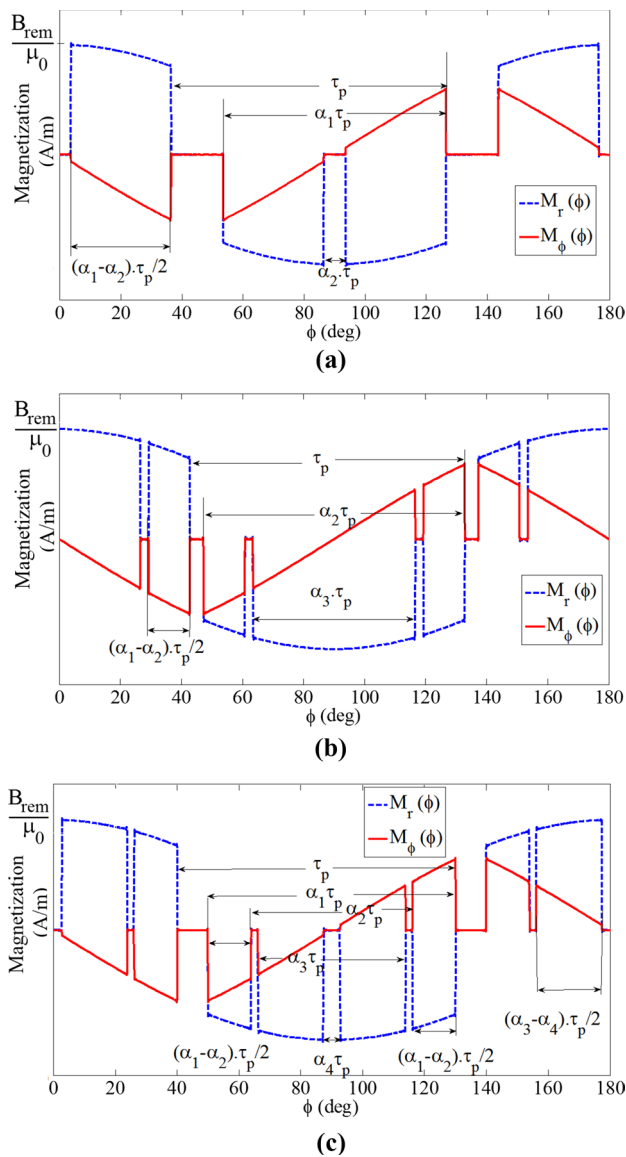


**Fig. 6** Magnetization of the structures with **a** two-, **b** three- and **c** four-segment parallel-magnetized PMs

four-segment PMs with the radial magnetization pattern are shown in Fig. 5a–c, respectively. In Fig. 6a–c, the magnetization of the two-, three- and four-segment parallel-magnetized PMs are shown, respectively. The Fourier coefficients of the magnetization function for two-, three- and four-segment radially magnetized PMs are obtained as (11), (12) and (13), respectively.

$$\begin{aligned}
 (M_{rcn}, M_{rsn}) &= \frac{2B_{rem}}{\mu_0 n \pi} (1 - \cos(n\pi)) \left( \sin\left(\frac{n\pi\alpha_1}{2}\right) - \sin\left(\frac{n\pi\alpha_2}{2}\right), 0 \right) \\
 M_\phi(r, \phi, \theta_r) &= 0
 \end{aligned}
 \tag{11}$$

$$\begin{aligned}
 (M_{rcn}, M_{rsn}) &= \frac{2B_{rem}}{\mu_0 n \pi} (1 - \cos(n\pi)) \left( \sin\left(\frac{n\pi\alpha_1}{2}\right) \right. \\
 &\quad \left. - \sin\left(\frac{n\pi\alpha_2}{2}\right) + \sin\left(\frac{n\pi\alpha_3}{2}\right), 0 \right) \\
 M_\phi(r, \phi, \theta_r) &= 0
 \end{aligned}
 \tag{12}$$

$$\begin{aligned}
 M_{rcn} &= \frac{2B_{rem}}{\mu_0 n \pi} (1 - (-1)^n) \left( \sin\left(\frac{n\pi\alpha_1}{2}\right) - \sin\left(\frac{n\pi\alpha_2}{2}\right) \right. \\
 &\quad \left. + \sin\left(\frac{n\pi\alpha_3}{2}\right) - \sin\left(\frac{n\pi\alpha_4}{2}\right) \right) \\
 M_{rsn} &= 0, M_\phi(r, \phi, \theta_r) = 0
 \end{aligned}
 \tag{13}$$

The Fourier coefficients of the magnetization function of the segmented parallel-magnetized PMs are expressed in (14).

$$\begin{aligned}
 [M_{rcn}, M_{srn}] &= (1 - \cos(n\pi)) p B_{rem} [U + V, 0] \\
 [M_{\phi cn}, M_{\phi sn}] &= (1 - \cos(n\pi)) p B_{rem} [0, U - V]
 \end{aligned}
 \tag{14}$$

where  $U$  and  $V$  for two-, three- and four-segment PMs are expressed in (15), (16) and (17), respectively.

$$U = \frac{\sin\left(\frac{(np+1)\alpha_1\pi}{2p}\right) - \sin\left(\frac{(np+1)\alpha_2\pi}{2p}\right)}{\mu_0\pi(np+1)}
 \tag{15}$$

$$V = \frac{\sin\left(\frac{(np-1)\alpha_1\pi}{2p}\right) - \sin\left(\frac{(np-1)\alpha_2\pi}{2p}\right)}{\mu_0\pi(np-1)}$$

$$U = \frac{\sin\left(\frac{(np+1)\alpha_1\pi}{2p}\right) - \sin\left(\frac{(np+1)\alpha_2\pi}{2p}\right) + \sin\left(\frac{(np+1)\alpha_3\pi}{2p}\right)}{\mu_0\pi(np+1)}$$

$$V = \frac{\sin\left(\frac{(np-1)\alpha_1\pi}{2p}\right) - \sin\left(\frac{(np-1)\alpha_2\pi}{2p}\right) + \sin\left(\frac{(np-1)\alpha_3\pi}{2p}\right)}{\mu_0\pi(np-1)}
 \tag{16}$$

$$U = \frac{\sin\left(\frac{(np+1)\alpha_1\pi}{2p}\right) - \sin\left(\frac{(np+1)\alpha_2\pi}{2p}\right) + \sin\left(\frac{(np+1)\alpha_3\pi}{2p}\right) - \sin\left(\frac{(np+1)\alpha_4\pi}{2p}\right)}{\mu_0\pi(np+1)}$$

$$V = \frac{\sin\left(\frac{(np-1)\alpha_1\pi}{2p}\right) - \sin\left(\frac{(np-1)\alpha_2\pi}{2p}\right) + \sin\left(\frac{(np-1)\alpha_3\pi}{2p}\right) - \sin\left(\frac{(np-1)\alpha_4\pi}{2p}\right)}{\mu_0\pi(np-1)}
 \tag{17}$$

### 3 Analytical modeling

In deriving the analytical model, the Poisson equation is solved by the method of the separation of variables. To consider the impact of the stator slots on the air gap flux density, the method in [15] is adopted. In this method, the slotted

SPM machine is replaced with a slotless machine and an equivalent magnetization current (EMC) sheet at the stator bore. The equivalent slotless machine is simply obtained by filling the slots of the slotted machine. In the analytical modeling process, the following assumptions are made.

- The PM relative magnetic permeability is 1.
- End effects and magnetic saturation are neglected.
- The two-dimensional Poisson equation is solved by the separation of the variables method.
- Both radially and parallel-magnetized PMs are studied.

The flowchart of the work is shown in Fig. 7. Since analytical expressions are provided for the electromagnetic variables, the algorithm converges very fast in only a few numbers of iterations.

In the used analytical model, the concept of the equivalent magnetizing current (EMC) is adopted for modeling of the slotted armature [15]. In this model, the no-load air gap flux density is due to the PMs and the EMCs as expressed in (18).

$$B_r(r, \varphi, \theta_r) = B_{rPM}(r, \varphi, \theta_r) + B_{rEMC}(r, \varphi, \theta_r)$$

$$B_\varphi(r, \varphi, \theta_r) = B_{\varphiPM}(r, \varphi, \theta_r) + B_{\varphiEMC}(r, \varphi, \theta_r) \tag{18}$$

The radial and circumferential components of the air gap flux density due to the PMs are as (19) and (20), respectively [15].

$$B_{rPM} = - \sum_{n=1,2,\dots}^{\infty} \frac{\mu_0}{r} (r^{np} + R_s^{2np} r^{-np}) \times [a_{cn} \cos(np(\varphi - \theta_r)) + a_{sn} \sin(np(\varphi - \theta_r))] \tag{19}$$

$$B_{\varphiPM} = \sum_{n=1,2,\dots}^{\infty} \frac{\mu_0}{r} (r^{np} - R_s^{2np} r^{-np}) \times [a_{cn} \sin(np(\phi - \theta_r)) - a_{sn} \cos(np(\phi - \theta_r))] \tag{20}$$

where  $a_{cn}$  and  $a_{sn}$  are defined in (21) and (22), respectively.

$$a_{cn} = \frac{np}{2(1 - (np)^2)(R_r^{2np} - R_s^{2np})} \times ((np + 1)(M_{rcn} + M_{\phi sn})R_r^{2np}R_m^{-np+1} + (1 - np)(M_{rcn} - M_{\phi sn})R_m^{np+1} - 2(M_{rcn} + npM_{\phi sn})R_r^{np+1}) \tag{21}$$

$$a_{sn} = \frac{np}{2(1 - (np)^2)(R_r^{2np} - R_s^{2np})} \times ((np + 1)(M_{rcn} - M_{\phi sn})R_r^{2np}R_m^{-np+1} + (1 - np)(M_{rcn} + M_{\phi sn})R_m^{np+1} - 2(M_{rcn} - npM_{\phi sn})R_r^{np+1}) \tag{22}$$

In addition, the radial component of the magnetic flux density in the stator back-iron due to the PMs is obtained as (23).

$$B_{rPM-stator}(r, \phi, \theta_r) = \sum_{n=1,2,\dots}^{\infty} \frac{-2\mu_0(r^{np} - R_o^{2np}r^{-np})}{r(1 - R_o^{2np}R_s^{-2np})} \times [a_{sn} \sin(np(\phi - \theta_r)) + a_{cn} \cos(np(\phi - \theta_r))] \tag{23}$$

To obtain the flux density caused by EMC in the slotless machine, the Poisson equation in the air gap region ( $R_r < R < R_s$ ) is solved, and the radial and circumferential components of the air gap flux density due to the EMC yield as (24) and (25), respectively.

$$B_{rEMC} = - \sum_{n=1,2,\dots}^{\infty} Y_n (r^{np-1} + R_r^{2np} r^{-np-1}) (J_{cn} \cos(np\phi) - J_{sn} \sin(np\phi)) \tag{24}$$

$$B_{\varphiEMC} = \sum_{n=1,2,\dots}^{\infty} Y_n (r^{np-1} - R_r^{2np} r^{-np-1}) (J_{sn} \sin(np\phi) + J_{cn} \cos(np\phi)) \tag{25}$$

where  $J_{sn}$  and  $J_{cn}$  are the sine and cosine Fourier coefficients of the EMC, and  $Y_n$  is defined in (26).

$$Y_n = \frac{-\mu_0 R_s^{np+1}}{R_r^{2np} - R_s^{2np}} \tag{26}$$

The radial magnetic flux density in the stator back-iron due to the EMC is obtained as (27), where  $C_n$  is defined in (28).

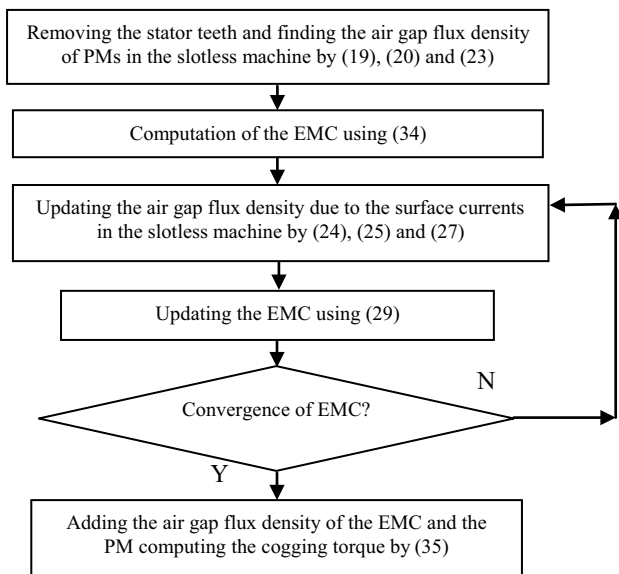


Fig. 7 Proposed algorithm of the modeling process

$$B_{rEMC-stator}(r, \phi, \theta_r) = \sum_{n=1,2,\dots}^{\infty} C_n(r) [J_{cn}(\theta_r) \cos(np\phi) - J_{sn}(\theta_r) \sin(np\phi)] \tag{27}$$

$$C_n(r) = Y_n \frac{R_r^{2np} + R_s^{2np}}{R_s^{2np} - R_o^{2np}} (r^{np-1} - R_o^{2np} r^{-np-1}) \tag{28}$$

As explained in [15], the EMC is obtained in an iterative algorithm with zero initial values. The Fourier series of the EMC is expressed in (29).

$$\begin{aligned} EMC(\theta_r, \phi) &= \sum_{n=1,2,\dots}^{\infty} J_{sn}(\theta_r) \sin(np\phi) + J_{cn}(\theta_r) \cos(np\phi) \\ J_{cn}(\theta_r) &= \sum_{i=1}^{Q_s/(p)} \zeta_n [J_{vi+}(\theta_r) \cos(npv_{i+}) + J_{vi-}(\theta_r) \cos(npv_{i-})] \\ J_{sn}(\theta_r) &= \sum_{i=1}^{Q_s/(p)} \zeta_n [J_{vi+}(\theta_r) \sin(npv_{i+}) + J_{vi-}(\theta_r) \sin(npv_{i-})] \\ \zeta_n &= \frac{4}{n\pi} \sin\left(\frac{np}{2} \Delta\theta\right) \end{aligned} \tag{29}$$

where  $J_{vi+/-}$  is the equivalent magnetizing surface current density at the right/left side of the  $i$ th slot. The values of  $v_{i+/-}$  and  $J_{vi+/-}$  are expressed in (30) and (31), respectively [15].

$$v_{i\pm} = \frac{(2i \mp 1)\gamma_s - \gamma_{so}}{2}, i = 1, 2, \dots, Q_s \tag{30}$$

$$J_{vi\pm}(\theta_r) = \pm \frac{(R_s - r)}{\Delta\theta \mu_0} \int_{R_s}^{R_s+h_{slot}} \frac{B_{rEMC-stator}(r, v_{i\pm}, \theta_r) + B_{rPM-stator}(r, v_{i\pm}, \theta_r)}{(x - r)} dx \tag{31}$$

where  $\Delta\theta$  is considered one-tenth of  $\gamma_{so}$ .

## 4 Multi-objective optimization

### 4.1 Objective function

Since analytical expressions are developed for the different PM arrangements, the direct search method is applied easily to find the optimum solutions. The used objective function is expressed in (32).

$$F = w_1 f_1 + w_2 f_2 \tag{32}$$

where  $f_1$  is the maxim value of the machine cogging torque,  $f_2$  is the THD the radial component of air gap flux density, and  $w_1$  and  $w_2$  are the considered weight for the functions  $f_1$  and  $f_2$ . The functions  $f_1$  and  $f_2$  are defined in (33) and (34).

$$f_1 = \max(T_{cog}) \tag{33}$$

$$f_2 = \frac{\sqrt{\sum_{i=2} B_{ri}^2}}{|B_{r1}|} = \frac{\sqrt{\sum_{i=2} B_{rsi}^2 + B_{rci}^2}}{|B_{r1}|} \tag{34}$$

where the subscript  $i$  denotes the  $i$ th harmonics in the radial component of the air gap flux density. Using the predicted air gap flux density components in the Maxwell stress tensor definition [16], the machine cogging torque is obtained as (35), where  $r$  is the radius of the Maxwell surface.

$$\begin{aligned} T_{cog}(\theta_r) &= \frac{L_{stk} r^2}{\mu_0} \int_0^{2\pi} B_r(r, \varphi, \theta_r) \cdot B_\varphi(r, \varphi, \theta_r) \cdot d\varphi \\ &= 2\pi p L_{stk} \sum_{n=1,2}^{\infty} Y_n (R_s^{2np} - R_r^{2np}) ((a_{cn} J_{cn} + a_{sn} J_{sn}) \sin(np\theta_r) \\ &\quad + (a_{sn} J_{cn} - a_{cn} J_{sn}) \cos(np\theta_r)) \end{aligned} \tag{35}$$

Since  $f_1$  and  $f_2$  are variables with different units, they have to be normalized before substituting in (33). The used method for the normalization is expressed in (36) [17].

$$g_{pu}(x) = \frac{g(x) - G_{min}}{G_{max} - G_{min}} \tag{36}$$

where  $g(x)$  is the desired function for normalization,  $x$  is the independent variable, and  $G_{min}$  and  $G_{max}$  are the minimum and maximum values of  $g$  over the search space domain.

**Table 1** Parameters of the considered SPM machine

Parameter	Symbol	Value
Machine pole pairs	$p$	2
Stator inner diameter	$R_s$	29.75 mm
Stator outer diameter	$R_o$	40 mm
Rotor radius	$R_r$	24.5 mm
Permanent magnet radius	$R_{pm}$	29 mm
Number of stator slots	$Q_s$	12
Machine stack length	$L_{stk}$	40 mm
Machine air gap length	$g$	0.75 mm
PM remnants flux density	$B_{rem}$	0.38 T
Slot height	$h_{slot}$	5 mm
PM thickness	$h_m$	4.5 mm
Slot opening distance	$b_0$	2 mm
Remnants of the strong PM	$B_{r2}$	0.38 T
Remnants of the weak PM	$B_{r1}$	0.25 T

**Table 2** Step and the range of the variation of the optimization variables

PMs arrangement	Variable	Step of changes	The range of the changes
The base arrangement	$\alpha$	0.01	[0.6 – 0.9]
PM shifting	$\alpha$	0.01	[0.6 – 0.9]
	$\alpha_0$	1°	[0 – (1 – $\alpha$ ) * 90°]
Mixed material PM	$\alpha_2$	0.01	$0.6 < 2\alpha_1 + \alpha_2 < 0.9$
	$\alpha_1$	0.01	$0.05 < \alpha_1$
Two-segment PM	$\alpha_1$	0.01	$0.6 < \alpha_1 - \alpha_2 < 0.9$
	$\alpha_2$	0.01	$0.05 < \alpha_2$
Three-segment PM	$\alpha_1$	0.01	$0.6 < \alpha_1 - \alpha_2 - \alpha_3 < 0.9$
	$\alpha_2$	0.01	$0.3 < \alpha_3$
	$\alpha_3$	0.01	$0.05 < \alpha_2 - \alpha_3$
Four-segment PM	$\alpha_1$	0.01	$0.6 < \alpha_1 - \alpha_2 - \alpha_3 + \alpha_4 < 0.9$
	$\alpha_2$	0.01	$0.3 < \alpha_3 - \alpha_4$
	$\alpha_3$	0.01	$0.05 < \alpha_2 - \alpha_3$
	$\alpha_4$	0.01	$0.05 < \alpha_4$

## 4.2 Optimization results

The predefined data of the considered SPM machine for the optimization process is reported in Table 1. The step and the range of the changes of the optimization variables in the different PM arrangements are reported in Table 2. The optimized variables and the related objective functions in the different PM arrangements with the radial and parallel magnetization patterns are reported in Table 3.

## 5 Result verification

In order to investigate the correctness of the obtained results, they are compared with FEA. Since the number of the investigated PM arrangements is high, due to the space limits, only some cases are investigated. All the illustrated results are for the optimized geometries reported in Table 3. In Fig. 8a and b, the air gap flux density components for the optimized PM-shifted structure with parallel and radial magnetizations are shown, respectively. The air gap flux density components for the optimized mixed material PM with parallel and radial magnetizations are illustrated in Fig. 8c and d, respectively.

The analytically obtained cogging torque, for the optimized machines with the PM-shifted arrangement, mixed material PM and three-segment and four-segment PMs, is shown in Fig. 9a–d, respectively. As shown in Fig. 9, the most effective method in cogging torque reduction is the simplest one, i.e., the PM shifting method. In addition, the mixed material PM arrangement is significantly more effective on the cogging torque mitigation than the PM segmentation. The cogging torque could be obtained by using the air flux density component and applying different methods such as Maxwell stress definition [16], energy derivation

**Table 3** Optimum values and the obtained objective functions for the different PM arrangements and different magnetization patterns

PM arrangement	Variables	Radially magnetized	Parallel magnetized
Base arrangement	$\alpha$	0.7	0.76
	$f_1$ (N m)	0.022	0.017
	$f_2$	23%	23%
	$F$	0	0.068
PM shifting	$\alpha$	0.69	0.74
	$\alpha_0$	4 (°)	4 (°)
	$f_1$ (N m)	0.003	0.007
	$f_2$	24.7%	25%
Mixed material PM	$F$	0.003	0.025
	$\alpha_1$	0.16	0.165
	$\alpha_2$	0.52	0.55
	$f_1$ (N m)	0.007	0.01
Two-segment PM	$f_2$	13%	11%
	$F$	0.047	0.014
	$\alpha_1$	0.76	0.81
	$\alpha_2$	0.06	0.08
Three-segment PM	$f_1$ (N m)	0.0134	0.0237
	$f_2$	39.5%	41.6%
	$F$	0.052	0.1488
	$\alpha_1$	0.7	0.95
Four-segment PM	$\alpha_2$	0.4	0.65
	$\alpha_3$	0.35	0.59
	$f_1$ (N m)	0.0503	0.0228
	$f_2$	27.3%	26.3%
Four-segment PM	$F$	0.2126	0.0441
	$\alpha_1$	0.87	0.89
	$\alpha_2$	0.57	0.58
	$\alpha_3$	0.51	0.53
Four-segment PM	$\alpha_4$	0.05	0.06
	$f_1$ (N m)	0.014	0.0131
	$f_2$	43%	37.6%
	$F$	0.1044	0.0409

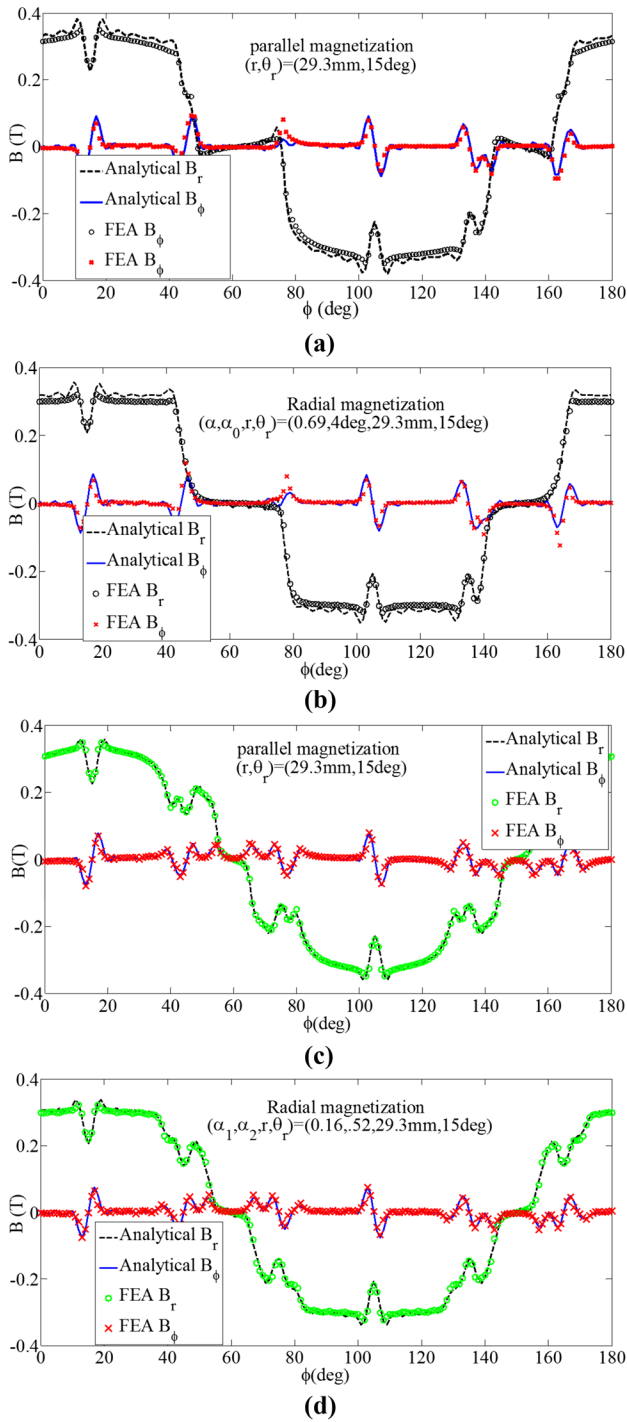


**Fig. 8** Air gap flux density components for **a** PM-shifted parallel-magnetized, **b** PM-shifted radially magnetized, **c** mixed material parallel-magnetized PMs, **d** mixed material radially magnetized PMs

[18] and the slot lateral force methods [19]. It should be noted that based on the method of flux density computation and other specifications of the used methods, the mentioned methods may result in different cogging torque waveform as discussed in [20].

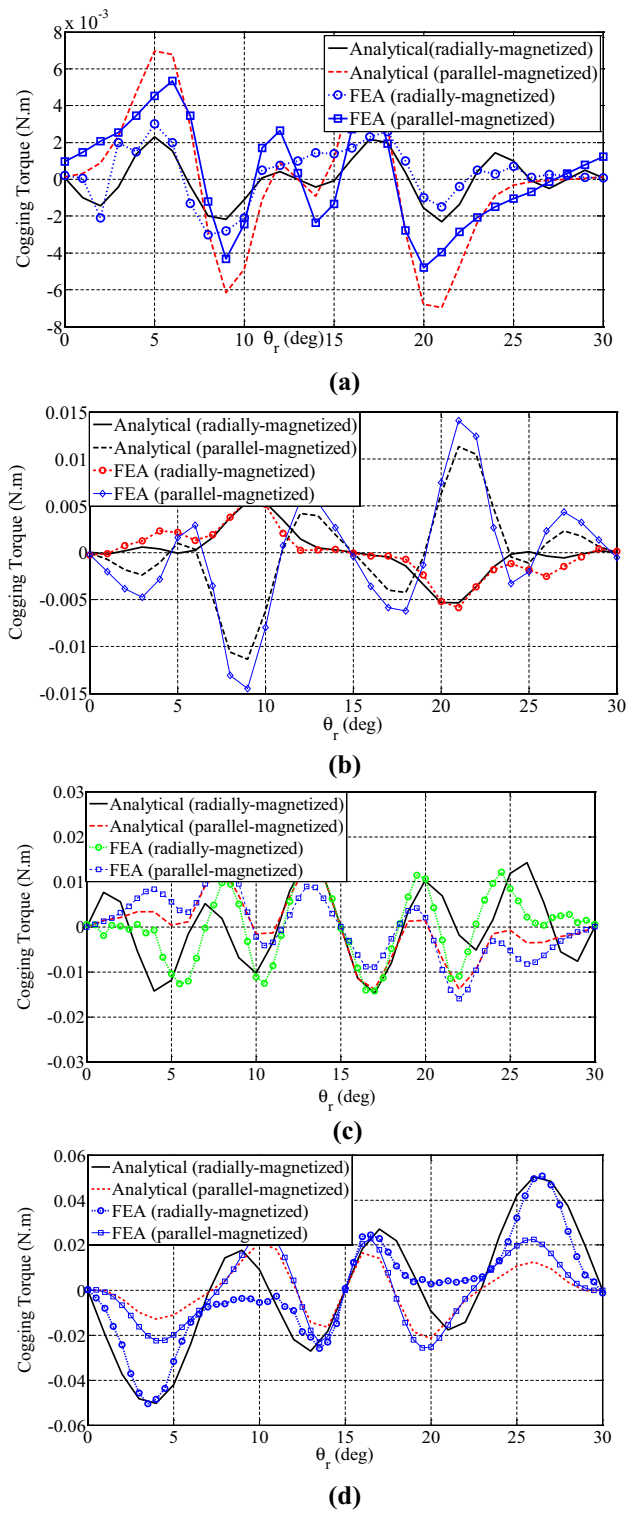


**Fig. 9** Cogging torque for **a** PM-shifted PM, **b** mixed material PM, **c** three-segment PM, **d** four-segment PM

Using the analytical model, the harmonic spectrum of the radial component of the air gap flux density is studied for different PM arrangements. In Fig. 10a and b, the harmonic

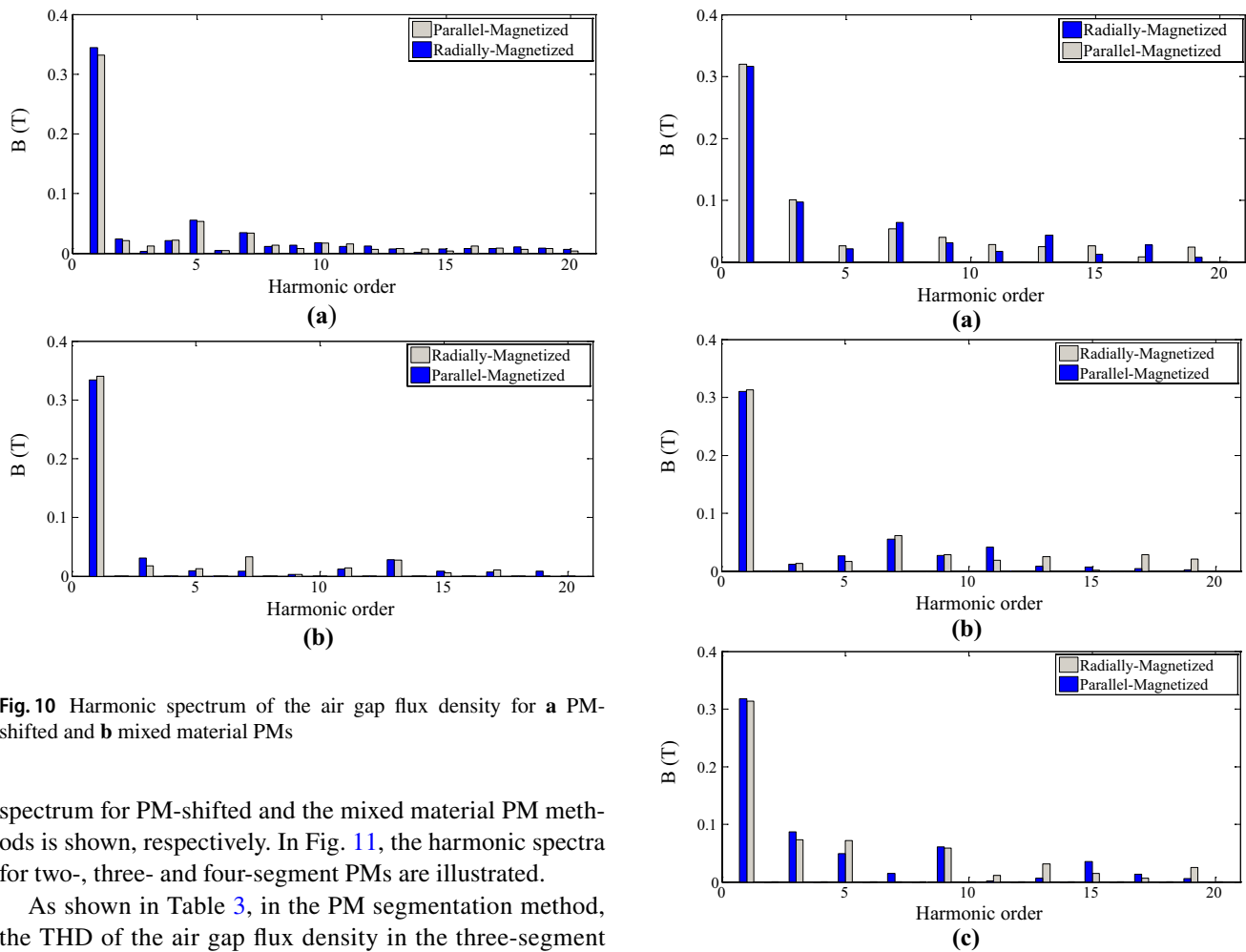


**Fig. 10** Harmonic spectrum of the air gap flux density for **a** PM-shifted and **b** mixed material PMs

spectrum for PM-shifted and the mixed material PM methods is shown, respectively. In Fig. 11, the harmonic spectra for two-, three- and four-segment PMs are illustrated.

As shown in Table 3, in the PM segmentation method, the THD of the air gap flux density in the three-segment PM is lower than the THD of the two- and four-segment PM arrangements. On the other hand, the machine cogging torque in the three-segment PM is higher than the cogging torque in the two- and four-segment PMs. In other words, a low value of the flux density THD does not result in a low value of cogging torque necessarily. In fact, the cogging torque depends on the derivative of the co-energy. The co-energy is a function of THD. Therefore, the cogging torque depends on the derivative of THD. It is obvious that the PM shifting method includes more harmonic contents.

Against the other PM arrangements, in the PM-shifted arrangement, the presence of the even harmonics is observable. In addition, the PM segmentation method increases, considerably, the harmonic content of the air gap flux density. Moreover, the mixed material PM arrangement is the best method as far as the harmonic spectrum is an important issue.

## 6 Conclusion

In this work, the SPM machine with different arrangements of the PMs is studied.

**Fig. 11** Harmonic spectrum of the air gap flux density for **a** two-, **b** three- and **c** four-segment PMs

The PM arrangements are optimized to reach a structure with a low value of the cogging torque and small THD of the radial component of the air gap flux density. The PM shifting method, PM segmentation method and the mixed material PMs are the studied arrangements. For this purpose, the geometry of the arrangements is formulated. By using an analytical model in a multi-objective optimization method, the geometries are optimized. Since the desired objective functions are not in the same unit, a normalization technique is used in the optimization process. Finally, the obtained results are verified with FEA. It is found that the PM segmentation method has no merit over the other PM arrangements. Although the PM shifting method is the most effective method in cogging torque reduction, its THD is high. Considering the cogging torque and the obtained THD in the air gap flux density, the mixed material PM arrangements are the best one.

**Acknowledgements** This research is carried out under the Grant Number 96GRD1M930 of the Shahrekord University.

## References

- Hwang SM, Eom JB, Hwang GB et al (2000) Cogging torque and acoustic noise reduction in permanent magnet motors by teeth paring. *IEEE Trans Magn* 36(5):3144–3146
- Zhu ZQ, Howe D (2000) Influence of design parameters on cogging torque in permanent magnet machines. *IEEE Trans Energy Convers* 15(4):407–412
- Wu L, Zhu ZQ (2014) Analytical modeling of surface-mounted PM machines accounting for magnet shaping and varied magnet property. *IEEE Trans Magn* 50(7):8101511
- Boroujeni ST, Zamani V (2016) Influence of magnet shaping on cogging torque of surface-mounted PM machines. *Int J Numer Model* 29(5):859–872
- Chen N, Ho SL, Fu WN (2010) Optimization of permanent magnet surface shapes of electric motors for minimization of cogging torque using FEM. *IEEE Trans Magn* 46(10):2478–2481
- Pang Y, Zhu ZQ, Feng ZJ (2011) Cogging torque in cost-effective surface-mounted permanent-magnet machines. *IEEE Trans Magn* 47(9):2269–2276
- Ruangsinchaiwanich S, Zhu ZQ, Howe D (2005) Influence of magnet shape on cogging torque and back-EMF waveform in permanent magnet machines. In: *Proceedings of 8th international conference on electrical machines and systems*, pp 284–289
- Yang Y, Wang X, Zhang R, Ding T, Tang R (2006) The optimization of pole arc coefficient to reduce cogging torque in surface-mounted permanent magnet motors. *IEEE Trans Magn* 42(4):1135–1138
- Bianchi N, Bolognani S (2002) Design techniques for reducing the cogging torque in surface-mounted PM motors. *IEEE Trans Magn* 38(5):1259–1265
- Islam MS, Sebastian T (2004) Issues in reducing the cogging torque on mass produced permanent magnet brushless Dc motor. *IEEE Trans Ind Appl* 40(3):813–820
- Lateb R, Takorabet N, Meibody Tabar F (2006) Effect of magnet segmentation on the cogging torque in surface-mounted permanent- magnet motors. *IEEE Trans Magn* 42(3):442–445
- Ashabani M, Abdel-Rady MY (2011) Multi-objective shape optimization of segmented pole permanent-magnet synchronous machines with improved torque characteristics. *IEEE Trans Magn* 47(4):795–804
- Shen Y, Zhu ZQ (2013) Analysis of electromagnetic performance of Halbach PM brushless machines having mixed grade and unequal height of magnets. *IEEE Trans Magn* 49(4):1461–1469
- Chaithongsuk S, Takorabet N, Meibody Tabar F (2009) On the use of pulse width modulation method for the elimination of flux density harmonics in the air-gap of surface PM Motors. *IEEE Trans Magn* 45(3):1736–1739
- Boroujeni ST, Zamani V (2015) A novel analytical model for no-load, slotted, surface-mounted PM machines: air gap flux density and cogging torque. *IEEE Trans Magn* 51(4):8104008
- Boroujeni ST, Jalali P, Bianchi N (2015) Analytical modeling of no-load eccentric slotted surface mounted PM machines: cogging torque and radial force. *IEEE Trans Magn* 30(2):754–760
- Varahram A, Mohassel JR, Mafinezhad K (2004) Optimization of array factor in linear arrays using modified genetic algorithm. *Int J Eng Trans B* 74(6):367–380
- Ebadi F, Mardaneh M, Rahideh A, Bianchi N (2019) Analytical energy-based approaches for cogging torque calculation in surface-mounted PM motors. *IEEE Trans Magn* 55(5):2906107
- Zarko D, Ban D, Lipo TA (2006) Analytical calculation of magnetic field distribution in the slotted air gap of a surface permanent-magnet motor using complex relative air-gap permeance. *IEEE Trans Magn* 42(7):1–8
- Wu LJ, Zhu ZQ, Staton DA, Popescu M, Hawkins D (2012) Comparison of analytical models of cogging torque in surface-mounted PM machines. *IEEE Trans Ind Electron* 59(6):2414–2425

**Publisher's Note** Springer Nature remains neutral with regard to jurisdictional claims in published maps and institutional affiliations.